Dynamic Response of Chiral Truss-core Assemblies

A. Spadoni, M. Ruzzene and F. Scarpa

Journal of Intelligent Material Systems and Structures 2006; 17; 941
DOI: 10.1177/1045389X06060219

Dynamic Response of Chiral Truss-core Assemblies

A. SPADONI,[1] M. RUZZENE[1,*] AND F. SCARPA[2]

[1]*School of Aerospace Engineering, Georgia Institute of Technology, Atlanta, GA, USA*

[2]*Department of Aerospace Engineering, The University of Bristol, Bristol, UK*

ABSTRACT: Periodic cellular configurations with negative Poisson's ratio have attracted the attention of several researchers because of their superior dynamic characteristics. Among the geometries with a negative Poisson's ratio, the chiral topology features localized deformed configurations when excited at one of its natural frequencies. This is of particular importance as resonance can be exploited to minimize the power required for the appearance of localized deformations, thus giving practicality to the concept. The particular nature of these deformed configurations and the authority provided by the chiral geometry suggest the application of the proposed structural configuration for the design of innovative lifting devices, such as helicopter rotor blades or airplane wings. The dynamic characteristics of chiral structures are here investigated through a numerical model and experimental investigations. The numerical formulation uses dynamic shape functions to accurately describe the behavior of the considered structural assembly over a wide frequency range. The model is used to predict frequency response functions, and to investigate the occurrence of localized deformations. Experimental tests are also performed to demonstrate the accuracy of the model and to illustrate the peculiarities of the behavior of the considered chiral structures.

Key Words: chiral structure, truss-core designs, dynamic shape control.

INTRODUCTION

In recent years, cellular structures have seen increased interest and applications due to their excellent mechanical properties and light weight characteristics (Gibson and Ashby, 1997). The application of stronger and lighter structural assemblies and materials is particularly relevant to the aircraft and aerospace industries, although many other applications can benefit from advances in materials and components. Ongoing interests in cellular structures and improvements in the manufacturing processes have contributed to the study and development of cellular solids of innovative shapes and topologies. Much interest has recently centered on cellular assemblies featuring a negative Poisson's ratio behavior, also known as 'auxetic' (Lakes, 1991). Materials having auxetic characteristics include special subsets of foams (Lakes, 1987), long-fiber composites (Alderson et al., 1997), microporous polymers (Lakes, 1991), as well as honeycombs (Scarpa and Tomlinson, 2000; Bornengo et al., 2005). The mechanical properties of these alternatives to solid components have thoroughly been investigated by (Zang and Ashby, 1991; Gibson et al., 1997; Evans et al., 2001; Wicks and Hutchinson, 2001) among others. In dynamics, specific attention has been placed on surface and Rayleigh wave propagation behavior in isotropic homogeneous linear elastic solids with negative Poisson's ratios (Lipsett and Beltzer, 1988). Among the proposed innovative geometries, chiral topologies (Lakes, 1991; Prall and Lakes, 1996) feature a unique geometric configuration which can be exploited for the design of innovative structural components. Chiral topologies have been also proposed as sources of negative Poisson's ratio effects in two-dimensional (2D) lattice models of hexagonal molecules at high density (Wojciechowski, 1989; 2003). Previous investigations by the authors have, in fact, shown how the chiral layout can be exploited for the design of sandwich panels with interesting structural acoustic behavior (Spadoni and Ruzzene, 2004), and as an alternative honeycomb configuration with superior flat-wise compression strength (Spadoni et al., 2005).

In the current work, the dynamic properties of truss-core assemblies with chiral core are investigated numerically and experimentally. The considered configurations are designed to generate deformed shapes, where the deformations are mostly localized in limited regions of the structure. These localized deformed shapes can be obtained through the excitation of the component at one of its resonant frequencies.

*Author to whom correspondence should be addressed.
E-mail: massimo.ruzzene@ae.gatech.edu
Figures 5–18 appear in color online: http://jim.sagepub.com

1045-389X/06/11 0941–12 $10.00/0 DOI: 10.1177/1045389X06060219

This is of particular importance as resonance can be exploited to minimize the power requirements, thus giving practicality to the concept. The feasibility of these concepts is investigated through a numerical formulation, which employs dynamic shape functions, derived directly from the distributed parameter model of beam elements. The analytical results are then compared to experimental measurements in an effort to validate the behavior observed in the numerical simulations.

This article is organized as follows: in the 'Concept and considered configurations' section an overview of the considered concept and objectives is presented. A description of the developed numerical model is offered in the 'Numerical model' section, which is followed by a discussion and comparison of both numerical and experimental results in the 'Dynamics shape control of a chiral truss-core beam' section. The 'Dynamic shape control of a chiral truss-core airfoil' section presents an extension of the proposed truss-core structures to be used in aerodynamic applications. The study concludes with a summary of the findings and an outline of future investigations required to fully explore the potentials of the considered geometry.

CONCEPT AND CONSIDERED CONFIGURATIONS

The class of structures proposed in the current work features a truss-type core with elements arranged according to a chiral topology. The unit cell defining the core is depicted in Figure 1. The unit cell is defined by ribs or walls connecting nodes or cylinders. The distance between the nodes is denoted as R, while the length of the ribs tangent to the nodes is L. Also, r and t are respectively the radius of the nodes and the wall thickness of all components. Finally, the angle between the lines connecting the node centers is denoted as θ, while the angle between the line connecting the nodes centers and the ribs is β. The following relationships defining the cell geometry hold (Prall and Lakes, 1996):

$$\sin\beta = \frac{2r}{R}, \quad \tan\beta = \frac{2r}{L} \tag{1}$$

For a hexagonal geometric layout θ is equal to 30°. Varying L, R, and t, produces a variety of core configurations and significantly alters the mechanical properties of the obtained assembly. The parameters L, R, and t are considered here as design variables which can be properly selected in order to obtain localized dynamic deformations.

The dynamic behavior of a simple sandwich beam configuration, depicted in Figure 2(a), is first investigated. The analysis is then extended to the airfoil-type configuration shown in Figure 2(b). The airfoil has been selected among standard shapes, while the core is obtained from a chiral geometry of the same layout as the one considered for the beam analysis. The chiral core is accommodated inside the airfoil structure to demonstrate the flexibility of the core topology to adapt to more complex shapes and applications. The dynamic characteristics of both geometries are investigated in terms of frequency–response functions. In the case of the truss-core beam, the excitation is realized through a harmonic point load, applied on one of the constraining layers, and a harmonic torque, applied on a core node. In the case of the truss-core airfoil, the excitation is represented by a harmonic strain induced at one of the ligaments of the core. Such excitation methods are employed to demonstrate how the considered core geometry can transfer induced strain at remote locations of the chiral-core assemblies.

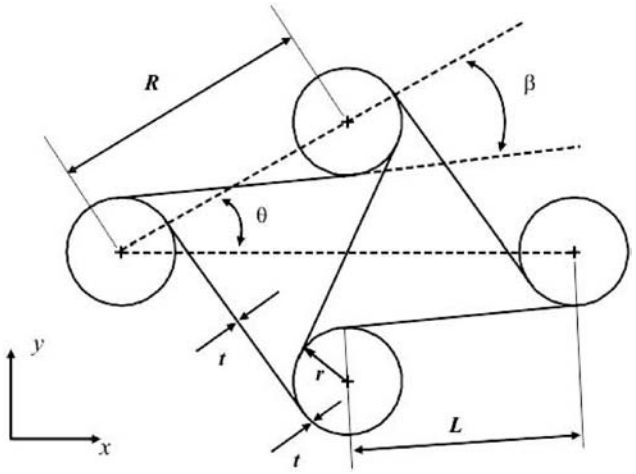

Figure 1. *Chiral geometry of a unit cell.*

NUMERICAL MODEL

The dynamic behavior of the truss-core panels is predicted by a model which describes the behavior of each element through dynamic equations derived from distributed parameter models (Doyle, 1988, 1997). This allows the accurate prediction of the dynamic response of the structure over a wide frequency range, without the need for refinement of the discretization as frequency increases. The considered sandwich beam is composed of rigidly connected beam elements, and thus is modeled as a frame structure with the circular nodes approximated as a sequence of straight beams. The elements are oriented in the plane of the structure x, y according to the core topology. The dynamic behavior of each element is described in the local reference system $\mathcal{L} = (\xi, \eta)$, rotated with respect to the global reference system $\mathcal{G} = (x, y)$ of the angle α (Figure 3). The model

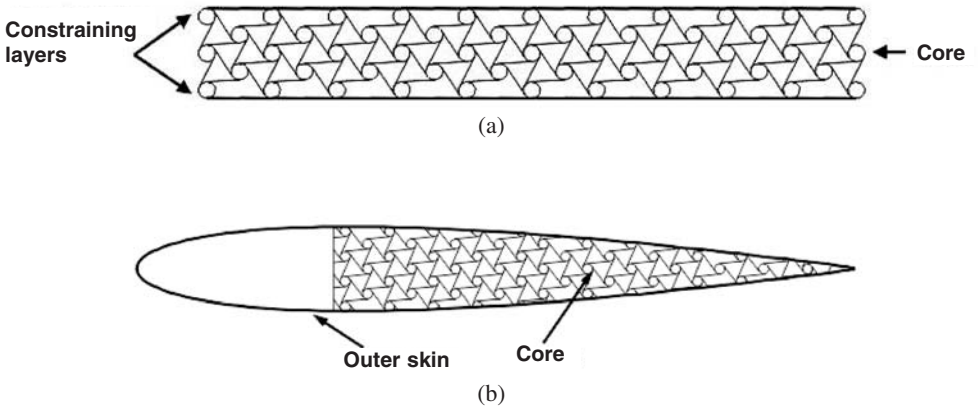

Figure 2. *Configurations considered (a) truss-core beam with chiral honeycomb core and (b) truss-core airfoil with chiral honeycomb core.*

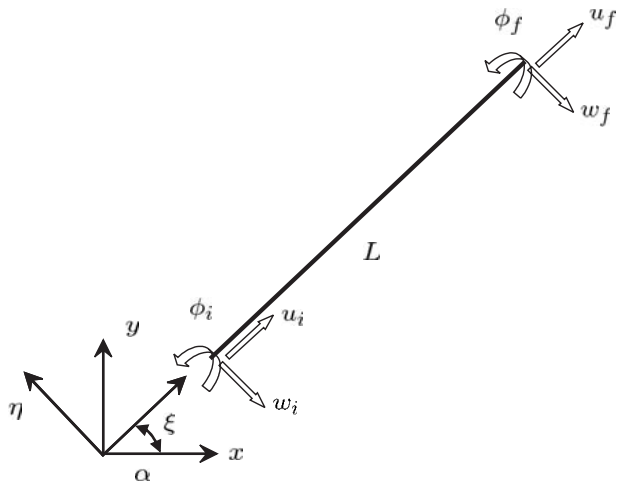

Figure 3. *Global and local reference systems with associated element degrees of freedom.*

contains elements of various lengths, some of which are very small. Timoshenko beam theory is thus considered to prevent lack of accuracy corresponding to the description of relatively short members through Euler–Bernoulli theory.

It is worth noting that while the basic linear elastic model proposed by Prall and Lakes describes an homogeneous isotropic linear elastic medium, the axial stiffness of the beam elements used in this work takes into account the deformation fields in 2D lattice networks and their special orthotropic behavior, both in centresymmetric and chiral assemblies (Gibson et al., 1997; Bornengo et al., 2005).

Distributed Parameter Model in the Local Reference System

The equations of motion and boundary conditions governing the longitudinal and transverse vibrations of a beam element can be derived by applying Hamilton's principle:

$$\int_{t_1}^{t_2} \delta(T - U + W)\,\mathrm{d}t = 0 \tag{2}$$

where, $\delta(.)$ denotes the first variation, t_1 and t_2 are the initial and final time, T and U are respectively the kinetic and the strain energy of the beam, and W is the work done by the external forces. Each element is considered as a Timoshenko beam, and includes axial degrees of freedom. In the local reference system, the beam's strain energy can be expressed as:

$$U = \frac{1}{2}\int_0^L \left[EAu_{,\xi}^2 + EI\phi_{,\xi}^2 + \kappa AG(w_{,\xi} - \phi)^2\right]\mathrm{d}\xi, \tag{3}$$

where E, G are the Young's and shear moduli, respectively, of the beam material, A, I are the area and the second moment of area of the beam cross section, respectively, and κ is the shear coefficient. Also, in Equation (3), $u = u(\xi, t), w = w(\xi, t)$ denote the axial and transverse deflection of the beam, while $\phi = \phi(\xi, t)$ is the rotation of the cross section at location ξ and time t. Finally, the following notation $(\diamond)_{,\xi} = \partial(\diamond)/\partial\xi$ is used to denote partial differentiation.

The kinetic energy is given by

$$T = \frac{1}{2}\int_0^L \left[\rho A(u_{,t}^2 + w_{,t}^2) + \rho I\phi_{,t}^2\right]\mathrm{d}x, \tag{4}$$

where ρ is the density of the beam material.

Dynamic Stiffness Matrix formulation

Substituting U and T in Equation (2), assuming the absence of external forces ($W = 0$), and performing the variations gives a set of three differential equations describing the beam's longitudinal and transverse vibration. For harmonic motion at frequency ω, the

equations of motion can be expressed in matrix form as follows:

$$\boldsymbol{z}_{,\xi}(\xi) = \boldsymbol{A}\boldsymbol{z}(\xi) \tag{5}$$

where $\boldsymbol{A}$ is a matrix of constant coefficients, and where

$$\boldsymbol{z} = \begin{bmatrix} u & w & \phi & u_{,\xi} & w_{,\xi} & \phi_{,\xi} \end{bmatrix}^T \tag{6}$$

is the state vector describing the axial and bending behavior of the considered beam element at frequency ω. In the current development, lower case bold letters indicate vectors, while capital bold case letters indicate matrices.

A general solution of Equation (5) can be expressed as:

$$\boldsymbol{z}(\xi) = e^{\boldsymbol{A}\xi}\boldsymbol{z}(0) \tag{7}$$

which relates the vector $\boldsymbol{z}$ at the generic location ξ to that at $\xi = 0$. An alternative expression for the state vector can be introduced to contain generalized displacements and stress resultants at the considered location. A vector $\boldsymbol{y}$ can be defined as:

$$\boldsymbol{y} = \begin{bmatrix} u & w & \phi & N & V & M \end{bmatrix}^T \tag{8}$$

where,

$$N(\xi) = EAu_{,\xi}, \quad V(\xi) = \kappa GA(w_{,\xi} - \phi), \quad M(\xi) = EI\phi_{,\xi}$$

are respectively the axial resultant, the shear force, and the bending moment at location ξ. The vectors $\boldsymbol{y}$ and $\boldsymbol{z}$ are simply related through the following expression:

$$\boldsymbol{y}(\xi) = \boldsymbol{G}\boldsymbol{z}(\xi) \tag{9}$$

where $\boldsymbol{G}$ is the constitutive matrix containing the material and cross sectional properties of the beam element. Equations (7) and (9) can be used to obtain a relation between state vectors at two locations on the element:

$$\begin{aligned} \boldsymbol{y}(\xi) &= \boldsymbol{G}e^{\boldsymbol{A}\xi}\boldsymbol{G}^{-1}\boldsymbol{y}(0) \\ \boldsymbol{y}(\xi) &= \boldsymbol{T}(\xi)\boldsymbol{y}(0) \end{aligned} \tag{10}$$

where $\boldsymbol{T}(\xi)$ is the 'transfer matrix' of the beam, calculated at location ξ. The transfer matrix can be used to relate generalized displacements and forces at the two ends of the element ($\xi = L$):

$$\boldsymbol{y}(L) = \boldsymbol{T}(L)\boldsymbol{y}(0) \tag{11}$$

Equation (11) then can be expanded as follows:

$$\begin{pmatrix} \boldsymbol{u}_f \\ \boldsymbol{f}_f \end{pmatrix} = \begin{pmatrix} \boldsymbol{T}_{11} & \boldsymbol{T}_{12} \\ \boldsymbol{T}_{21} & \boldsymbol{T}_{22} \end{pmatrix} \begin{pmatrix} \boldsymbol{u}_i \\ \boldsymbol{f}_i \end{pmatrix} \tag{12}$$

where $\boldsymbol{u}_i, \boldsymbol{u}_f$ and $\boldsymbol{f}_i, \boldsymbol{f}_f$ respectively are the generalized displacements and forces at the initial and final node. Equation (12) can be rearranged to obtain:

$$\boldsymbol{f}_e^{\mathcal{L}} = \boldsymbol{K}_{d_e}^{\mathcal{L}}\boldsymbol{u}_e^{\mathcal{L}} \tag{13}$$

where $\boldsymbol{f}_e^{\mathcal{L}} = (\boldsymbol{f}_i \ \boldsymbol{f}_f)^T$, $\boldsymbol{u}_e^{\mathcal{L}} = (\boldsymbol{u}_i \ \boldsymbol{u}_f)^T$, and where $\boldsymbol{K}_{d_e}^{\mathcal{L}}$ is the dynamic stiffness matrix of the element, which is obtained as:

$$\boldsymbol{K}_{d_e}^{\mathcal{L}} = \begin{pmatrix} -\boldsymbol{T}_{12}^{-1}\boldsymbol{T}_{11} & \boldsymbol{T}_{12}^{-1} \\ \boldsymbol{T}_{21} - \boldsymbol{T}_{22}\boldsymbol{T}_{12}^{-1}\boldsymbol{T}_{11} & \boldsymbol{T}_{22}\boldsymbol{T}_{12}^{-1} \end{pmatrix} \tag{14}$$

In Equation (13), the subscript e denotes vectors pertaining to the element, while superscript $\mathcal{L}$ indicates that the expression is obtained in the local reference system $\mathcal{L} = (\xi, \eta)$. The generalized displacements of points within the element are expressed in terms of the nodal degrees of freedom:

$$\boldsymbol{u}(\xi) = \mathbf{N}(\xi)\boldsymbol{u}_e^{\mathcal{L}} \tag{15}$$

where $\mathbf{N}(\xi)$ is the matrix of the dynamic interpolation functions, which is obtained from the transfer matrix formulation given above.

The dynamic stiffness matrix for the element is obtained from the beam's distributed parameter model for harmonic motion at frequency ω. Within the validity of Timoshenko approximations, the model reproduces the exact displacements of the considered element. Accordingly, a single finite element is sufficient to fully characterize the response of a beam.

The components of the beam's longitudinal and transverse displacements u, w in the global reference system $\mathcal{G} = (x, y)$ are given in terms of the rotation angle α in Figure 3. The dynamic stiffness formulation in the global reference system $\boldsymbol{K}_{d_e}^{\mathcal{G}}$ is defined in terms of the stiffness matrix in local coordinates through a rotation matrix defined in term of the angle α.

Assembly for all the elements of the truss-core beam yields the discretized equation of motion for the considered structure, which has the well known form:

$$\boldsymbol{f} = \boldsymbol{K}_d\boldsymbol{u} \tag{16}$$

where $\boldsymbol{u}, \boldsymbol{f}$, and $\boldsymbol{K}_d$ are the vector of the degrees of freedom of the entire structure, the vector of the equivalent external nodal loads, and the assembled dynamic stiffness matrix. Solution of the equation for an assigned set of external loads at given frequency yields the amplitude of the displacements at each node. The displacements within each element can then be obtained through the general elemental solution and the dynamic interpolation functions described by Equation (15).

DYNAMIC SHAPE CONTROL OF A CHIRAL TRUSS-CORE BEAM

The ability to obtain useful deformed configurations with low input power levels, and the authority provided by the chiral geometry offer an alternative to more traditional morphing concepts. Shape control of structural components can be achieved by employing

active materials, such as electroactive polymers (EAP) (Bar Cohen, 2001), or mechanisms composed of actuators. In the former case, the material may not be suitable for load-carrying applications, while the latter case may be difficult to implement, as actuators usually require a control system and add significant mass. Consequently, chiral truss-core assemblies are proposed as a novel technique to obtain useful deformed configurations, as they offer a scalable geometry, and thus a scalable frequency response, low energy input requirements, and multifunctional characteristics, whereby load-carrying and dynamic shape control capabilities may be combined.

The numerical model described in the previous section is first used to predict the dynamic response of the truss-core beam shown in Figure 4(a). The baseline configuration features two identical constraining layers of thickness $t_{b1} = 0.81\,\text{mm}$, and a core of thickness $t_c = 6.9\,\text{cm}$. The total length of the beam is $L_b = 0.5\,\text{m}$. Both the core and constraining layers are made of aluminum (Young's Modulus $E = 7.1\text{e}10\,\text{N/m}^2$, density $\rho = 2700\,\text{kg/m}^3$, Poisson's ratio $\nu = 0.33$). The chiral configuration is characterized by the following parameters (Figure 1): $R = 2.82\,\text{cm}$, $r = 0.56\,\text{cm}$, $L = 2.59\,\text{cm}$, $\theta = 30^\circ$, $\beta = 26.9^\circ$. The wall thickness of the ligaments is 0.81 mm, while the wall thickness of the nodes is 0.89 mm. The beam is fixed at the right end and free at the left end. Finally, the out-of-plane thickness is 2.54 cm.

Numerical Results

The capabilities of chiral truss-core configurations are investigated using two excitation strategies, shown in Figure 4. In the first configuration, a harmonic point load is applied to one of the constraining layers, near the clamped end of the beam. The excitation frequency is varied from 0 to 2000 Hz, to cover a wide range of structural resonances. The response of the beam is first evaluated in terms of frequency-response functions (FRF). The FRF for the free-tip displacement of top and bottom layers is plotted in Figure 5. As originally pointed out by (El-Raheb, 1997; Ruzzene, 2004), the behavior of truss-core beams can be divided into frequency regions which strongly depend upon geometry and material properties. At low excitation frequencies, the behavior of this class of structures may be treated as that of an equivalent homogeneous beam, and the deformed shapes are characterized by similar displacements for top and bottom layers. In this frequency range, the influence of the core topology is only limited to increasing or decreasing the bending stiffness of the complete assembly, and the dynamic response may be reasonably predicted by homogenization techniques (Noor, 1988; Lok and Cheng, 2000). Examples of the deformed configurations at frequencies belonging to the low frequency region, are depicted in Figure 6(a) and (b), which respectively shows the operational deflection shapes corresponding to the first two natural frequencies. The end of the low-frequency region is signaled by intracell resonance (Ruzzene, 2004), as the wavelength becomes of the order of the core elements' length. At these excitation regimes, equivalent homogenization fails (Noor, 1988) and the entire assembly with all its core complexity must be analyzed. Intracell resonance is here investigated as the phenomenon responsible for complex deformation patterns, observed in this class of structures. A selection of deformed configurations featuring intracell resonance is shown in Figure 6(c) and (d). In particular, at the selected frequencies local deformations appear on the constraining layers. This phenomenon then is the focus of the experimental validation, and more generally, of the current study.

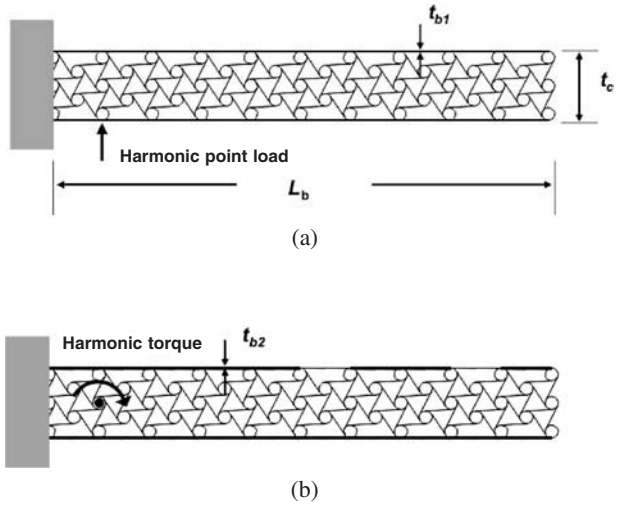

Figure 4. *Beam configuration and schematic of excitation.*

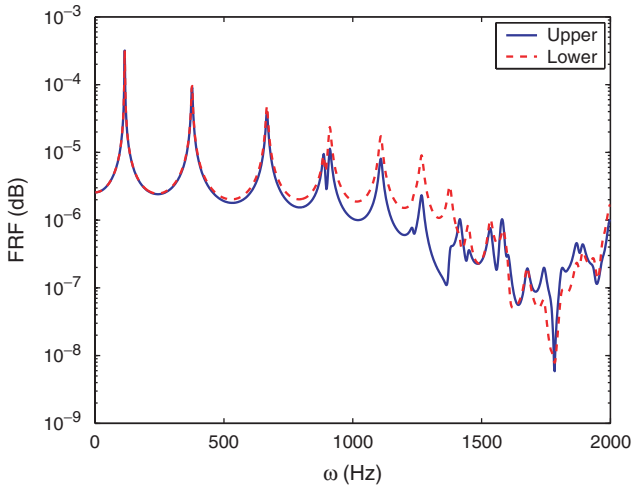

Figure 5. *Frequency–response function of the free end of the beam for an applied harmonic point load (upper and lower constraining layers).*

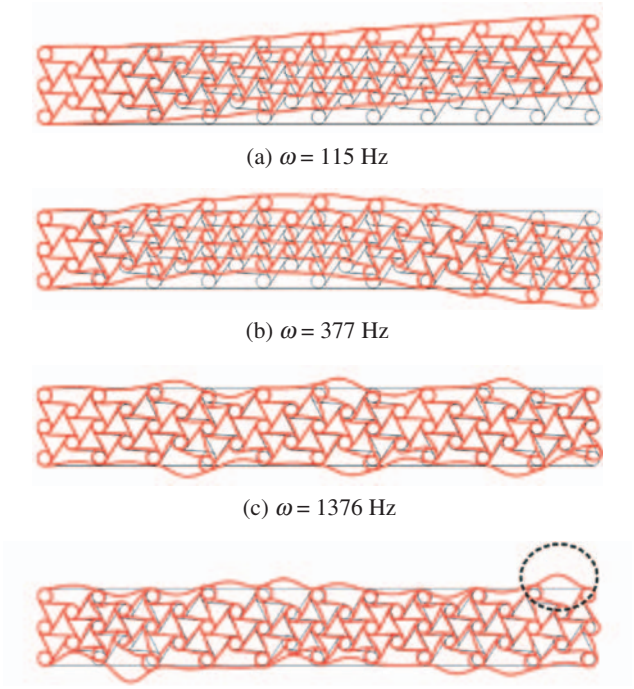

(a) $\omega = 115$ Hz

(b) $\omega = 377$ Hz

(c) $\omega = 1376$ Hz

(d) $\omega = 1533$ Hz

Figure 6. *Deformed configurations for the point-load case, for low and high-frequency excitation regimes.*

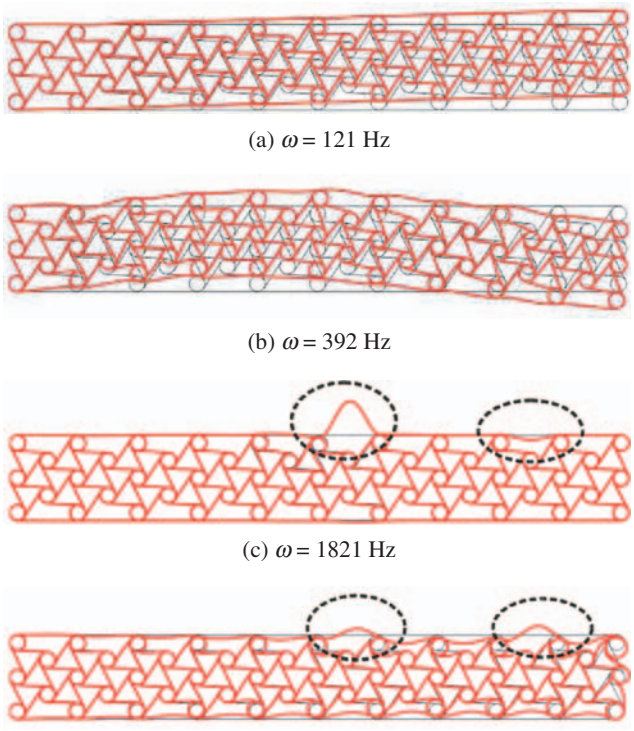

(a) $\omega = 121$ Hz

(b) $\omega = 392$ Hz

(c) $\omega = 1821$ Hz

(d) $\omega = 2386$ Hz

Figure 7. *Deformed configurations for the harmonic-torque case for low- and high-frequency excitation regimes.*

The second excitation configuration shown in Figure 4(b), is characterized by an applied harmonic torque on one of the core circular nodes. The thickness of top and bottom layers $t_{b1} = 0.81$ mm is doubled to $t_{b2} = 1.62$ mm, while specific locations of the top layer maintain the original thickness value of t_{b1}. The design modifications were considered in an effort to facilitate the occurrence of localized deformations on the constraining layers. All other geometric dimensions and material properties remain equal to the case of an applied point load. The structural layout presented in Figure 4(b) then possesses higher bending stiffness. In order to properly characterize the modal behavior of the truss-core structure, the range of excitation frequencies is now extended to 3000 Hz. The deformed configurations for the low frequency region are depicted in Figure 7(a) and (b) which represent the operational deflection shapes for the first two natural frequencies. As for the case of point-load excitation at low excitation frequencies, the deformed configurations are similar to those of a homogeneous beam. At higher excitation regimes, the typical deformed configurations shown in Figure 7(c) and (d), are observed. Increasing the constraining layers' thickness from t_{b1} to t_{b2}, while maintaining wall thickness t_{b1} for the two locations on the upper layer shown in Figure 4(b), allows to isolate and control the occurrence of localized deformations. Furthermore, by controlling the excitation frequency, the location and phase of the same localized deformations may be varied in a controlled manner.

EXPERIMENTAL VALIDATION

Overview

A proof of concept truss-core beam has been built with the objective of demonstrating the particular dynamic behavior of chiral assemblies. Geometry and materials for the experimental specimen have been selected with the goal of maintaining simplicity of fabrication while utilizing off-the-shelf components.

Truss-core Fabrication

The radius r of the nodes, the length of the ribs, and the wall thickness of both ribs and nodes are chosen to allow bending deformation of the ribs with low deformation of the nodes. This is a necessary condition to ensure the peculiar 'unfolding' behavior of deformed chiral honeycombs (Lakes, 1991; Prall and Lakes, 1996). Both the core ribs and the constraining layers are fabricated from standard alloy 6061 T6 aluminum sheet (Young's modulus $E = 7.0$ GPa, density $\rho = 2700$ Kg/m^3, Poisson's ratio $\nu = 0.33$). The ribs are 2.90 cm long, and have a wall thickness of 0.81 mm, which corresponds to the standard thickness of 0.032 in. in aluminum sheets. The nodes are fabricated from aluminum tubing of diameter 1.11 cm (7/16 in.), with wall thickness $t = 0.89$ mm (0.035 in.). The top and bottom constraining layers are 49.24 cm long and their wall thickness is

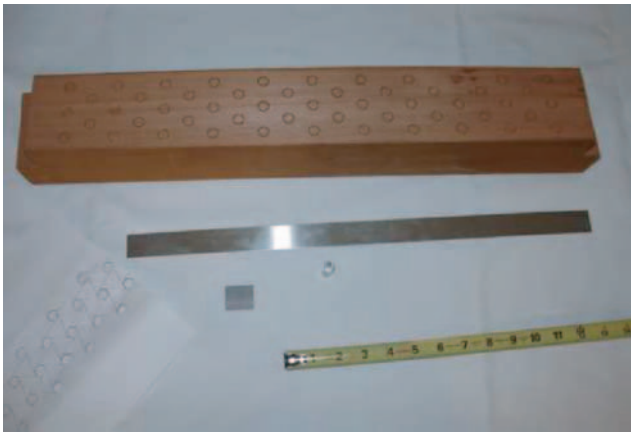

(a)

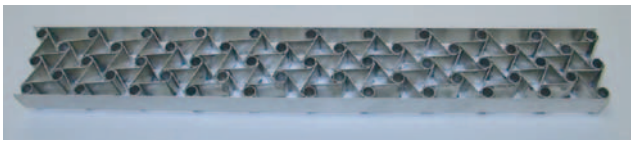

(b)

Figure 8. *(a) Wooden template and (b) completed assembly.*

equal to 0.81 mm. Finally, the out-of-plane thickness of the structure is equal to 2.54 cm. Given these dimensions and the geometry shown in Figure 4, the parameter L becomes equal to 2.59 cm, while the distance between the nodes R is equal to 2.82 cm. Due to the thickness of the ribs, the ratio L/R decreases from a nominal value of 0.919 to 0.892. The complete truss-core beam is composed of 53 nodes and 112 ribs. The overall dimensions of the structure are $L_b = 0.5$ m and $t_c = 6.9$ cm.

The experimental specimen was assembled by first constructing a wooden template to ensure correct positioning of the nodes (Figure 8(a)). The nodes were then placed in the template at the correct locations. Finally, the constraining layers and ribs were welded to the nodes using the 3M epoxy adhesive DP − 190 to obtain the completed assembly shown in Figure 8(b).

Experimental Set-up

The structure is constrained at one end by two vices which rigidly clamp both the core and the constraining layers. The measurement setup shown in Figure 9(a) consists of the Polytec PSV-400 laser scanning head, the Polytec PSV-400 M2 data acquisition system and signal processing, a LDS V203 shaker, and a 10 lb force transducer, mounted on the shaker's stinger. The shaker excites the structure according to a prescribed forcing function, so that the excitation methods presented in section 'Dynamic shape control of a chiral truss-core beam' can be experimentally replicated. The case of a point load is simulated by exciting the structure with the

(a)

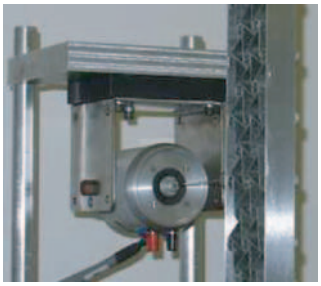

(b)

Figure 9. *(a) Experimental setup and testing equipment and (b) point-load excitation configuration.*

shaker placed approximately 14.5 cm from the clamped end of the assembly (Figure 4(b)). In order to simulate the case of an applied torque, a threaded steel axle is inserted in one of the core nodes, and it is secured to the assembly with nuts. A solid steel plate 2.4 cm long is welded on one end of the steel axel. The shaker then applies a load on the steel plate as shown in Figure 10(a). The torque imparted on the core of the assembly is then given by the load imposed by the shaker and the moment arm R. Such setup is shown in Figure 10(b). Finally, the vibration of the structure is characterized by measuring the velocity of points belonging to a 1281-point measurement grid on the constraining layer facing the laser head.

Experimental Results and Discussion

As for the analytical simulations presented in the 'Dynamic shape control of a chiral truss-core beam' section, the experimental response of the truss-core beam is first evaluated in terms of frequency–response functions. The comparison of FRF for the analytical and experimental simulations is shown in Figure 11. The measured response at low frequencies compares well with the numerical simulations. The effects introduced by the epoxy adhesive, however, produce disagreement between the analytical and experimental models at high

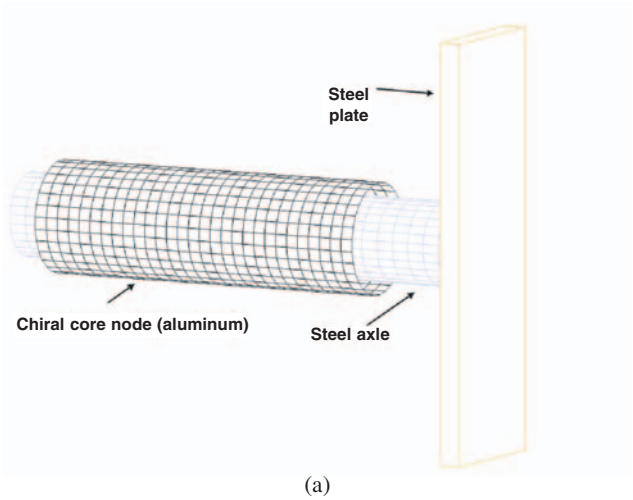

(a)

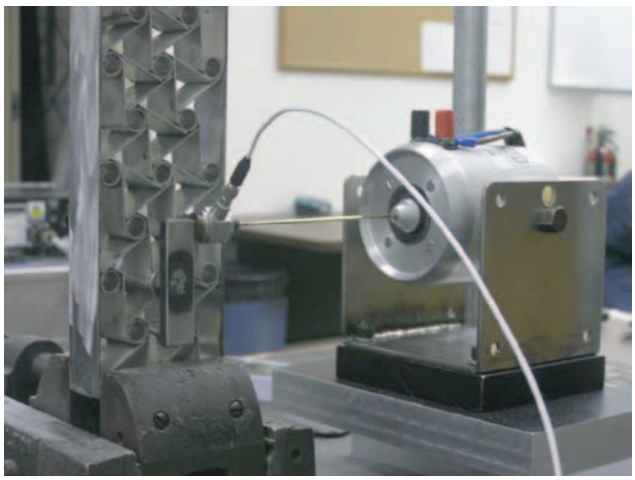

(b)

Figure 10. *(a) Mechanism for torque actuation at one node and (b) detail of shaker mounting.*

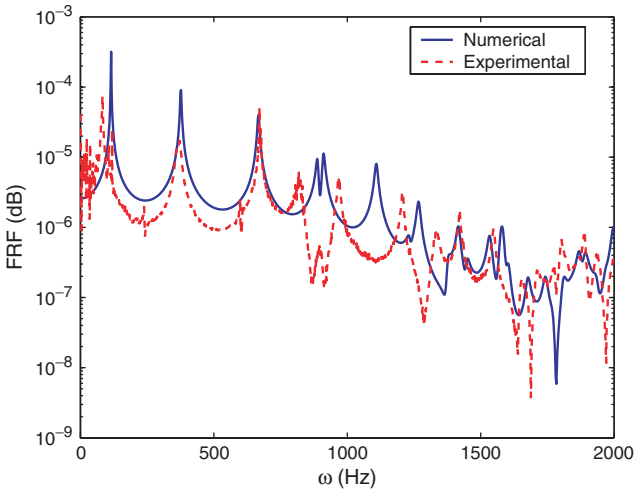

Figure 11. *Experimental and analytical frequency–response function of the free end of the beam for an applied point load.*

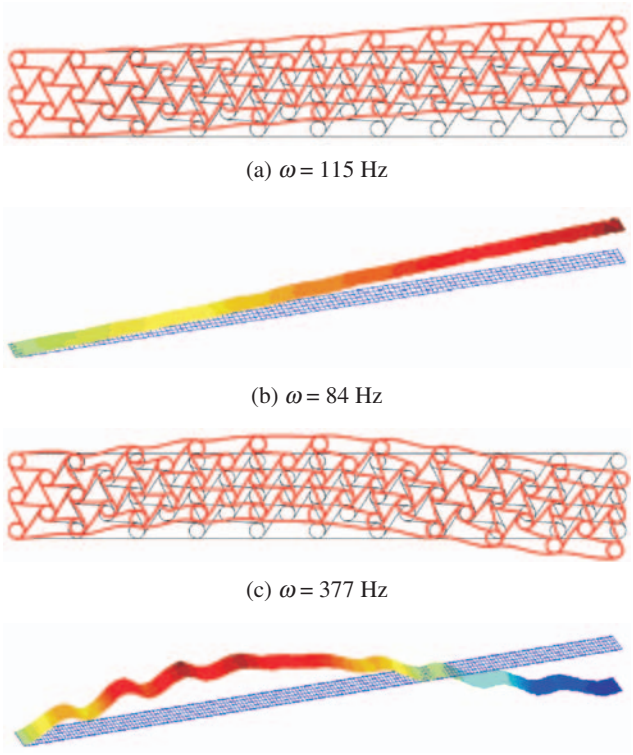

(a) $\omega = 115$ Hz

(b) $\omega = 84$ Hz

(c) $\omega = 377$ Hz

(d) $\omega = 358$ Hz

Figure 12. *Experimental (b,d) and numerical (a,c) operational deflection shapes for a point-load excitation.*

excitation regimes. Furthermore, some of the natural frequencies observed experimentally between 750 and 1250 Hz correspond to torsional modes which are not modelled analytically. In the model, structural damping is introduced by defining the Young's modulus as $E = 7.1\text{e}10(1 + i \cdot \eta)$, where η is chosen to be 0.02 for the core components and equal to 0.01 for the constraining layers. These values are selected by trial and error to obtain a reasonable match with the experimental results. Figure 12 shows a comparison between measured and analytical operational deflection shapes, at frequencies belonging to the low frequency regime. The phenomenon of intracell resonance is demonstrated by the deformed configurations shown in Figure 13. Specifically, at $\omega = 1546$ Hz the experimental model produces a marked kink at the free end of the beam, while the rest of the constraining layer is much less deformed. The deformed shape of the constraining layer obtained from the numerical model for $\omega = 1536$ Hz (Figure 13(c)), on the other hand, appears much more corrugated. Overall, however, agreement between the numerical and experimental results is acceptable at frequencies up to approximately 1110 Hz.

The increase in layer thickness from t_{b1} to t_{b2} is investigated experimentally as well. These design modifications are implemented by bonding strips of aluminum sheet with the 3M epoxy adhesive DP – 190, to obtain the configuration shown in Figure 4(b). The layer

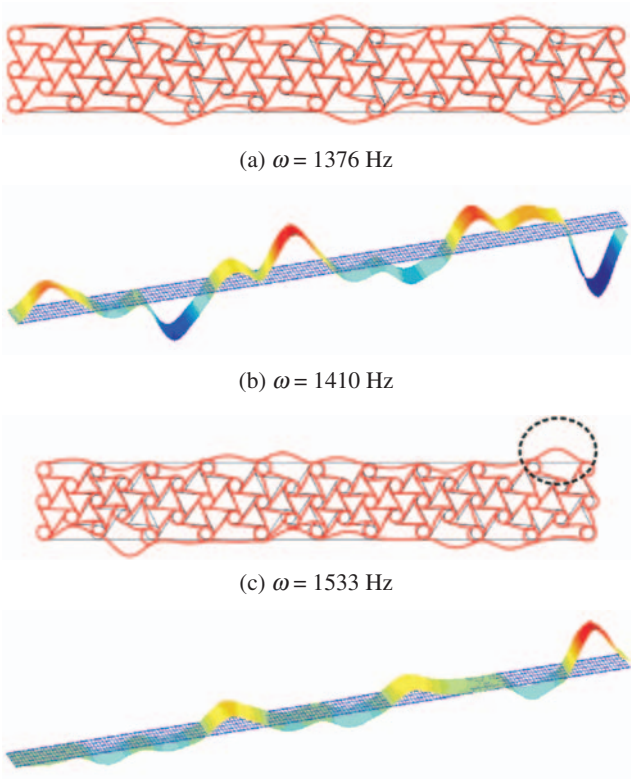

(a) $\omega = 1376$ Hz

(b) $\omega = 1410$ Hz

(c) $\omega = 1533$ Hz

(d) $\omega = 1546$ Hz

Figure 13. *Experimental (b,d) and numerical (a,c) operational deflection shapes for a point-load excitation.*

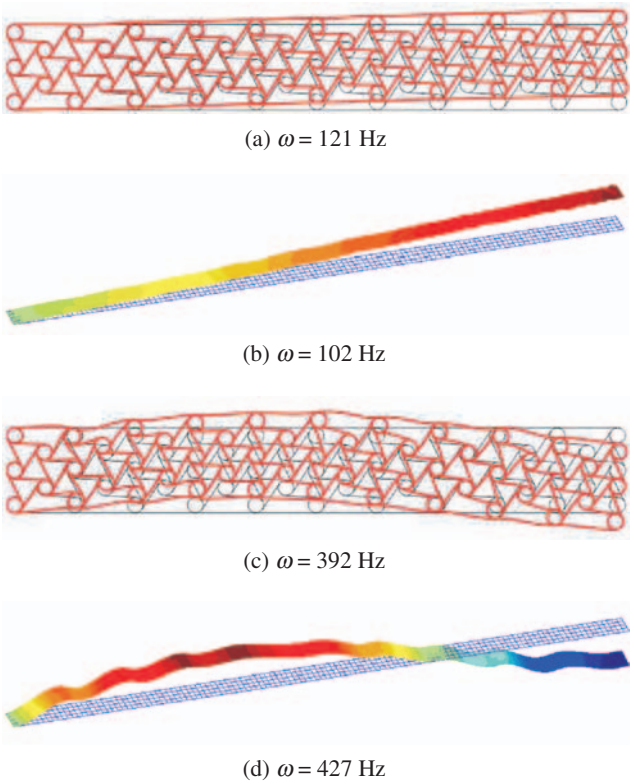

(a) $\omega = 121$ Hz

(b) $\omega = 102$ Hz

(c) $\omega = 392$ Hz

(d) $\omega = 427$ Hz

Figure 14. *Experimental (b,d) and numerical (a,c) operational deflection shapes for the case of an applied torque to a core node.*

thickness t_{b2} is now 1.61 mm. For an applied torque to one of the core nodes, the dynamic response in the low frequency range is similar to case of an applied point load; although the deformed configurations corresponding to the first two natural frequencies, depicted in Figure 14, occur at higher frequencies. Similarly, intracell resonance takes place at higher excitation regimes. The deformed profiles typical of intracell resonance, however, present very well marked localized deformations near the free end of the beam, as shown in Figure 15. The rest of the constraining layers, as opposed to the case of layer thickness t_{b1}, appear nearly undeformed.

The unique behavior of chiral truss-core beams observed from numerical and experimental analyses shows that, when the excitation frequency is such that wavelengths become of the order of the core components' length, energy is transfered from the location of excitation to specific locations on the constraining layers, without generating global deformations, as shown in Figures 12–15. The onset of intracell resonance is determined by natural frequencies corresponding to specific geometric and constitutive parameters. This suggests that the actuation frequencies producing localized deformations may be scaled to favor particular operation deflection shapes for a given application. Finally, localized deformations on the constraining

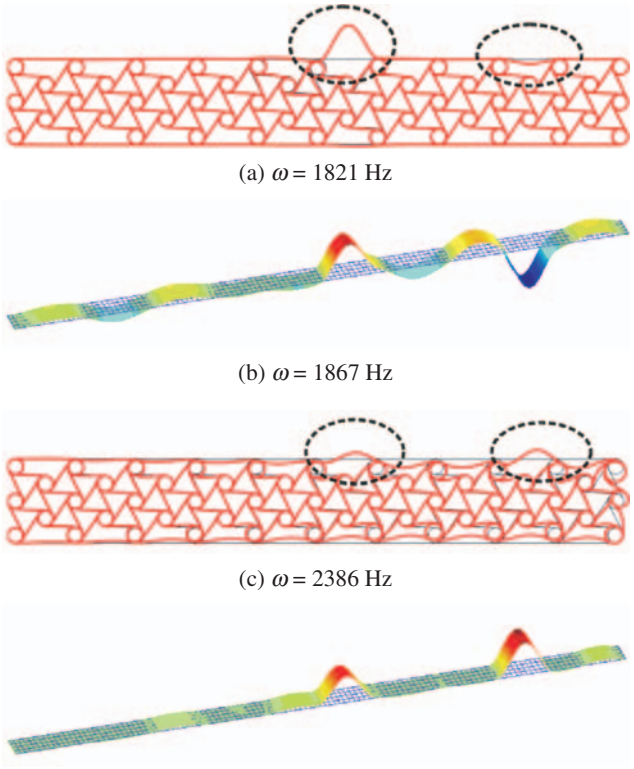

(a) $\omega = 1821$ Hz

(b) $\omega = 1867$ Hz

(c) $\omega = 2386$ Hz

(d) $\omega = 2027$ Hz

Figure 15. *Experimental (b,d) and numerical (a,c) operational deflection shapes for the case of an applied torque to a core node.*

layers appear to be a dominant characteristic of the dynamic response of chiral-core assemblies, since two distinct forcing frequencies, for example, produce localized deformations (Figure 15) with opposite phase. This indicates that the onset of different types of local deformations can be simply controlled by changing the excitation frequency.

DYNAMIC SHAPE CONTROL OF A CHIRAL TRUSS-CORE AIRFOIL

In the previous section, the ability of the novel core geometry to transfer strain or energy to remote locations, without producing global deformation, was presented. An illustration of the potential of such capabilities is presented here in the form of an airfoil whose core is composed of the chiral geometry. Localized deformed shapes of the kind here investigated could be relevant, for example, for the improvement of the performance of an airfoil through modification of flow patterns (Chandrasekhara et al., 1997). The realization of this concept requires the deformations to be controllable. This can be achieved by designating a ligament or a node as 'active'. The insertion of energy in the structure can thus be achieved by non-intrusive means, since the portion to be actuated can be far away from the location where shape control is needed.

Although, so far, this is a conceptual configuration, it well demonstrates the possible advantages of being able to tailor a wing profile dynamically. A traditional means of controlling the flow around an airfoil is steady blowing at locations, where the flow is likely to separate or create bubbles (Lissaman, 1983). The advantages of constant blowing over airfoils have been thoroughly presented in the literature, and have been utilized in short-take-off aircraft. Recently however, the same principles of flow control have been expanded to pulsating or unsteady blowing (Honohan et al., 2000). The effect of such actions on an airfoil is to transfer momentum to the surrounding flow, and to enhance the bound circulation (circulation around the airfoil). Similar results can be achieved by mechanical momentum transfer through pulsating deformations of the airfoil. The demonstration of such phenomena can be found, for example, in (Chandrasekhara et al., 1997; Munday and Jamey, 2001), among others. The localized deformations illustrated in the previous sections may be used as a means for transfering mechanical momentum to the flow.

The airfoil shown in Figure 16, is the standard NACA 0012, with a chord, $c = 2\,\mathrm{m}$. The leading edge is considered as rigid, and only the aft section of the airfoil is modeled as a truss-core assembly. For conceptual purposes, the outer skin is made of a stiffer material than the core ($t_b = 3\,\mathrm{mm}$, Young's Modulus $E = 2.2\mathrm{e}11\,\mathrm{N/m^2}$, density $\rho = 7800\,\mathrm{Kg/m^3}$, Poisson's ratio $\nu = 0.33$). The internal core of the airfoil is aluminum ($t = 1.5\,\mathrm{mm}$, Young's Modulus $E = 7.1\mathrm{e}10\,\mathrm{N/m^2}$, density $\rho = 2700\,\mathrm{Kg/m^3}$, Poisson's ratio $\nu = 0.33$). The geometric parameters of the chiral core are maintained equal to those used previously. The core element on which the harmonic strain is applied is shown in Figure 16. The location of the active element is chosen in an effort to demonstrate that deformations of the outer skin may take place far away from the actuation site.

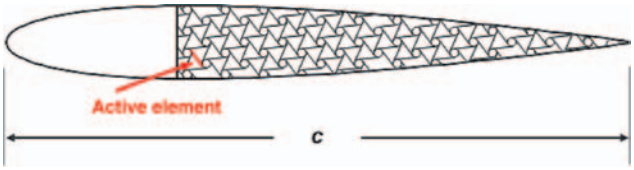

Figure 16. *Truss-core airfoil with active ligament.*

Dynamic Shape Control through Localized Actuation

The actuation strategy devised for the truss-core airfoil is such that an axially induced harmonic strain, ϵ_a, is applied to the core ligament shown in Figure 16. The work done by the induced strain can be expressed as:

$$W^{(e)} = \int_0^{L^{(e)}} AE\epsilon_a \mathrm{d}\xi, \tag{17}$$

where, in light of the development presented in 'Numerical model' section, the induced strain can be recast to produce the following relation:

$$W^{(e)} = \int_0^{L^{(e)}} AE\boldsymbol{B}\mathrm{d}\xi \quad \boldsymbol{u}_e^{\mathcal{L}} = \boldsymbol{f}_e^{\mathcal{L}^T}\boldsymbol{u}_e^{\mathcal{L}}, \tag{18}$$

where $\boldsymbol{f}_e^{\mathcal{L}}$ is the elemental load vector expressed in the local reference frame, while $\boldsymbol{B}$ is the strain interpolation matrix, which can be obtained as follows:

$$\boldsymbol{B} = \mathbf{b}\boldsymbol{N}_{,\xi}(\xi), \tag{19}$$

where $\mathbf{b}$ is a boolean matrix that selects the appropriate components of the shape function matrix to obtain the axial strain, ϵ_a. Finally, as for the nodal displacements, the elemental load vector expressed in the global reference system is obtained as $\boldsymbol{f}_e^{\mathcal{L}} = \boldsymbol{R}\boldsymbol{f}_e^{\mathcal{G}}$.

The deformations associated with the truss-core airfoil present a variety of useful configurations, which may be exploited for both flow separation and lift control purposes. In particular, the deformed configurations corresponding to the first and second natural frequencies (Figure 17(a) and (b)), consisting mainly of global in-plane bending, may be used to modify the effective camber of a wing. The deformed configurations depicted in Figure 18(a–d), on the other hand, are a result of core intracell resonance, whereby strain is

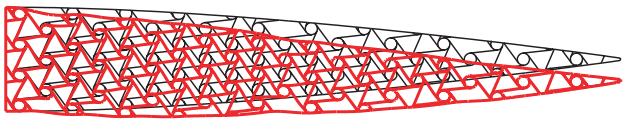

(a) $\omega = 101$ Hz

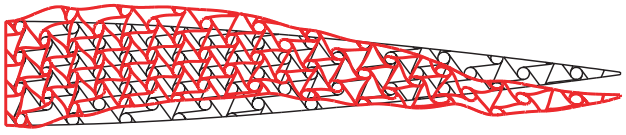

(b) $\omega = 246$ Hz

Figure 17. *Deformed configurations of the truss-core airfoil for low-frequency excitation regimes.*

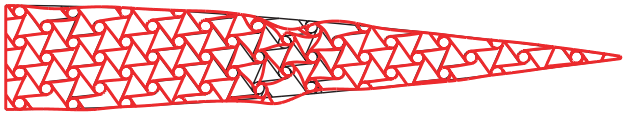

(a) $\omega = 637$ Hz

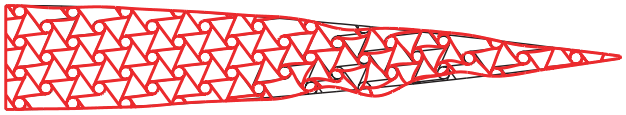

(b) $\omega = 705$ Hz

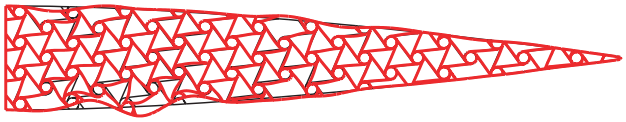

(c) $\omega = 750$ Hz

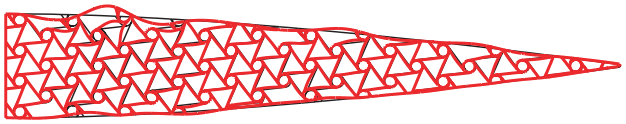

(d) $\omega = 768$ Hz

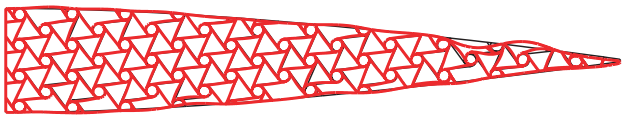

(e) $\omega = 816$ Hz

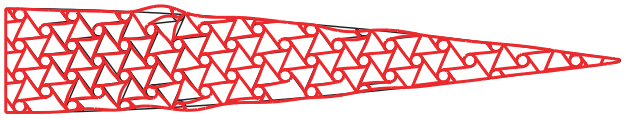

(f) $\omega = 903$ Hz

Figure 18. *Deformed configurations of the truss-core airfoil for high-frequency excitation regimes.*

transfered from the active ligament to the outer skin. The particular response of the truss-core assembly, for such actuation regimes, presents local deformations on the outer skin of which various locations can be excited by changing the forcing frequency.

CONCLUSION

The dynamic response of chiral truss-core assemblies is investigated numerically and experimentally. The complexity of the chiral topology guarantees a variety of useful deformations, as a result of harmonic excitation. Two actuation methods are presented: a point load on one of the constraining layers of the beam, and the torque actuation of a core node. The insertion of energy in the structure, in principle, can be achieved by non-intrusive means, since the portion to be actuated can be far away from the location where shape control is needed. Consequently, chiral truss-core assemblies are proposed as novel configurations to obtain useful operational deflection shapes, as they offer a scalable geometry without increasing weight, potential for low energy input requirements, and multifunctionality. The unique deformation characteristics of chiral truss-core structures are demonstrated both numerically and experimentally on a cantilevered truss-core beam configuration and explored numerically on an airfoil design. The agreement between experiments and numerical predictions gives confidence for future investigations, where the applications of the proposed concept for aerodynamic applications will be explored.

ACKNOWLEDGMENTS

This work is supported by the grant W911NF0410141 from the Army Research Office. The authors wish to thank Dr Gary Anderson, program manager and technical monitor, for his support and invaluable technical inputs.

REFERENCES

Alderson, K.L., Alderson, A. and Evans, K.E. 1997. "The Interpretation of the Strain-dependent Poisson's Ratio in Auxetic Polyethylene," *J. Strain Analysis*, 32:201–212.

Bar Cohen, Y. 2001. "Electroactive Polymers (EAP) as Artificial Muscles," SPIE Press, Bellingham, WA.

Bornengo, B., Scarpa, F. and Remillat, C. 2005. "Evaluation of Hexagonal Chiral Structure for Morphing Airfoil Concept," In: *proceedings of IMEchE Part G: Journal of Aerospace Engineering*, 3:185–192.

Chandrasekhara, M.S., Carr, L.W., Wilder, M.C., Paulson, G.N. and Sticht, C.D. 1997. "Design and Development of a Dynamically Deforming Leading Edge Airfoil for Unsteady Flow Control," *IEEE Publication 97CH36121*, 132–140.

Doyle, J.F. 1988. "A Spectrally-formulated Finite Element for Longitudinal Wave Propagation," *Int. Journal of Analytical and Experimental Modal Analysis*, (3):1–5.

Doyle, J.F. 1997. *Wave Propagation in Structures*, 2nd ed, Springer Verlag, New York, NY.

El-Raheb, M. 1997. "Frequency Response of a Two-dimensional Trusslike Periodic Panel," *Journal of the Acoustic Society of America*, 101(6):3457–3465.

Evans, A.G., Hutchinson, J.W., Fleck, N.A., Ashby, M.F. and Wadley, H.N.G., 2001. "The Topological Design of Multifunctional Cellular Metals," *Progress in Materials Science*, 46:309–327.

Gibson, L.J. and Ashby, M.F. 1997. "Cellular Solids: Structure Properties," 2nd ed, Cambridge University Press, Cambridge, UK.

Honohan, A.M., Amitay, M. and Glazer, A. 2000. "Aerodynamic Control using Synthetic Jets," In: *Fluids 2000, AIAA 2000-2541, Denver, CO*.

Lakes R.S. 1987. "Foam structures with a Negative Poisson's Ratio," *Science*, 235:1038–1040.

Lakes R.S. 1991. "Deformation Mechanisms in Negative Poisson's Ratio Materials: Structural Aspects," *J. Mat. Sci*., 26:2287–2292.

Lissaman, P.B.S., 1983. "Low-Reynolds-Number Airfoils," *Annual Review of Fluid Mechanics*, (15):223–239.

Lipsett, W. and Beltzer, A. 1988. "Reexamination of dynamic problems of elasticity for negative Poisson's ratio," *J. Acoust. Soc. Am. 84*, 2179:2179–2186.

Lok, T.S. and Cheng, Q.H. 2000. "Free Vibration of Clamped Orthotropic Sandwich Panel," *Journal of Sound and Vibration*, 229(2):311–327.

Munday D. and Jamey J. 2001. "Active Control of Separation on a Wing with Conformable Camber," In: *39th AIAA-2001-0293 Aerospace Sciences Meeting and Exhibit, Reno*, NV.

Noor, A.K. 1988. "Continuum modeling for repetitive lattice structures," *Apllied Mechanics Reviews*, 41(7):285–296.

Prall, D. and Lakes, R.S. 1996. "Properties of a Chiral Honeycomb with Poisson's Ratio of -1," *Int. J. of Mechanical Sciences*, 39:305–314.

Ruzzene, M. 2004. "Vibration and Sound Radiation of Sandwich Beams with Honeycombs," *Journal of Sound and Vibration*, 277:741–763.

Scarpa, F. and Tomlinson, G. 2000. "Theoretical Characteristics of the Vibration of Sandwich Plates with In-plane Negative Poisson's Ratio Values," *Journal of Sound and Vibration*, 230(1):45–67.

Spadoni, A. and Ruzzene, M. 2004. "Structural and Acoustic Behavior of Chiral Trusscore Beams," *Procedings of the ASME (IMECE 2004) Noise Control and Acoustic Division*, November 2004, Anaheim, CA.

Spadoni, A., Ruzzene, M. and Scarpa, F. 2005. "Global and Local Linear Buckling Behavior of a Chiral Cellular Structure," *Physica Status Solidi (b)*, 242(3):695–709.

Wicks, N. and Hutchinson, J.W. 2001. "Optimal Truss Plates," *International Journal of Solids and Structures*, 38:5165–5183.

Wojciechowski, K.W. 1989. "Two-dimensional Isotropic System with a Negative Poisson's Ration," *Physics Letters A*, 137:60–64.

Wojciechowski, K.W. 2003. "Non-chiral, Molecular Model of Negative Poisson ratio in Two Dimensions," *Phys. A: Math. Gen*., 36(47):11765-11778.

Zang, J. and Ashby, M.F. 1991. *The Out-of-Plane Properties of Honeycombs*, Cambridge University Press, Cambridge, UK.